

## Research Article

# Analysis of Fatigue Crack Propagation of an Orthotropic Bridge Deck Based on the Extended Finite Element Method

Ying Wang , Zhen Wang, and Yuqian Zheng

*Jiangsu Key Laboratory of Engineering Mechanics, Southeast University, Nanjing 21009, China*

Correspondence should be addressed to Ying Wang; [civil\\_wangying@seu.edu.cn](mailto:civil_wangying@seu.edu.cn)

Received 6 May 2019; Accepted 7 July 2019; Published 25 July 2019

Academic Editor: Rafael J. Bergillos

Copyright © 2019 Ying Wang et al. This is an open access article distributed under the Creative Commons Attribution License, which permits unrestricted use, distribution, and reproduction in any medium, provided the original work is properly cited.

As one of the most fatigue-sensitive parts of an orthotropic steel bridge deck, the weld between the U-rib and the top deck is prone to fatigue cracking under the actions of the stress concentration, welding residual stress, and vehicle load. To investigate the mechanism of fatigue crack propagation and the influence of the welding residual stress on the propagation patterns of fatigue cracks, a multiscale modeling method was proposed, and the static analysis and the dynamic propagation analysis of fatigue crack were carried out in this paper. First, a multiscale finite element model was established, including whole bridge models with a scale feature of  $10^2$  m, orthotropic bridge deck models with a scale feature of  $10^0$  m, and crack models with a scale feature of  $10^{-3}$  m. Then, a segmental model of the bridge deck was extracted, which is regarded as a critical location of the bridge, and the shell-solid coupling method is adopted in the segmental model in order to further analyze the crack propagation rule. Moreover, based on the extended finite element method (XFEM), the static crack and dynamic crack propagation in this critical position were analyzed. Finally, thermoelastoplastic analysis was carried out on the connection of the U-rib and deck with a length of 500 mm to obtain the residual stress, and then the results of residual stress were introduced into the segmental model to further study its influence on the evolution of fatigue crack propagation. The analysis of the welding process shows that near the weld region of the connection of the U-rib and deck, the peak value of the residual tensile stress can reach the material yield strength. The static analysis of fatigue cracks shows that under the single action of a standard fatigue vehicle load, the fatigue details at the weld toe of the deck cannot reach the tensile stress required for fatigue crack propagation, and only the fatigue details at the weld toe of the U-rib can meet the requirements of fatigue crack propagation. The dynamic analysis of fatigue cracks reveals that the crack in the weld toe of the U-rib is a mixed-mode crack with modes I, II, and III. The propagation of a fatigue crack without a residual stress field will be terminated until the crack length is extended to a certain length. Nevertheless, when the residual stress field was introduced, the growth angle and size of the fatigue crack would increase, and no crack closure occurs. For the crack in the weld toe of the deck, the crack is in the closed state under the standard fatigue vehicle load. When the residual stress field is introduced, the tensile stress of the fatigue details increases. Meanwhile, the fatigue crack will become a mixed-mode crack with modes I, II, and III that will be dominated by mode I and extend toward the weld at a slight deflection angle. The results of various initial crack sizes at the weld toes of the top deck are analyzed, which shows that the initial crack size has a certain effect on the fatigue crack growth rate, especially the initial crack depth.

## 1. Introduction

The orthotropic steel bridge deck is the preferred deck structure for long-span steel bridges and is widely used in modern bridges due to its light weight, construction convenience, performance stability, etc. Nevertheless, as a result of the structural complexities, crowded welds, and stress concentration problems, the deck structure is prone to

fatigue failure under the repeated action of a vehicle load. According to the investigation results of the fatigue and fracture subcommittee of the American Society of Civil Engineering (ASCE), 80–90% of steel structure damage is related to fatigue, and the fatigue fracture has become one of the main reasons for steel bridge failure [1]. To investigate the fatigue of a steel bridge deck, fatigue tests and numerical simulation methods have been adopted in many studies.

Numerical simulation has been proven to be very useful due to its repeatability, low cost, and visualization of the interior structure [2]. At present, there are two numerical simulation methods to study the fatigue performance of orthotropic bridges. One method is based on the stress-life curve (S-N curve) evaluation method, while the other method is based on the fracture mechanics method. However, the S-N curve method has certain serious drawbacks, such as the method neglecting the initial material defects and considering only the stage before crack initiation, and its incapability of describing fatigue crack propagation [3]. It has been proven that the evaluation method based on fracture mechanics has inherent advantages in predicting the fatigue life of steel bridges [4], which can overcome the deficiency of the evaluation based on the S-N curve method.

In recent years, the fracture mechanics method has been widely used in numerical simulations of macroscopic crack propagation processes and fatigue life analyses of orthotropic steel bridge decks. The extended finite element method (XFEM) is a new finite element method and was first proposed by Belyschko and Black at Northwestern University in 1999. This method is used to solve the problem of describing crack propagation in the FE method by using the idea of independent mesh division. The method does not need remeshing for the internal cracks and other defects in the analysis process and can retain all of the advantages of traditional finite elements. Zhang et al. [5] proposed a three-dimensional fatigue crack propagation simulation method suitable for elliptical or semielliptical cracks. Combined with a full-scale fatigue test, this method was used to study the crack propagation evolution and fatigue life of the welding details at the longitudinal rib and top deck of an orthotropic steel bridge. According to the full-scale fatigue test of the orthotropic steel deck, Wang et al. [6] found that due to the influence of the welding residual stress, fatigue cracks also occurred at the welding seam between the top deck and the diaphragm plate, i.e., the compressive stress zone under fatigue load. Subsequently, Wang et al. [7] introduced the welding residual stress field into the segmental model of the steel bridge deck and studied the typical detailed fatigue cracking mechanism and crack growth behavior of a steel bridge deck under a residual stress field based on the theory of linear elastic fracture mechanics (LEFM), the Paris formula, and the XFEM. Nagy et al. [8, 9] used the theory of LEFM and the XFEM to evaluate the fatigue life of steel bridges, analyzed the quantitative relation between the fatigue crack growth length and the stress intensity factor (SIF) amplitude at the welding root of the joint of the U-rib and top deck, and obtained the fatigue life under a residual stress field with the Paris formula. Wang et al. [10] adopted a homogenization treatment for the random defects in the weld heat-affected zone with the criterion of the equivalent length of crack propagation, used the XFEM to calculate the SIF of the equivalent crack propagation length, and obtained the macroscopic crack initiation life according to the modified Paris formula, considering the random defects at the joint of the U-rib and top deck. Du and Shi [11] modified the parameters of the Paris formula and adopted a four-step method to study the propagation evolution of surface cracks

in the welding seam between the U-rib and deck under cyclic loads, considering the influence of the compressive stress. The welding residual stress at the welding seam has a significant influence on the average value and the maximum value of the cyclic stress in the bridge deck and affects the fatigue performance of the bridge deck. However, there is a lack of detailed studies on the influence of the residual stress field on the fatigue crack propagation mechanism and evolution. There is no quantitative analysis on the influences of the initial crack length and depth on fatigue crack propagation under a residual stress field.

Therefore, based on the XFEM, the fatigue crack propagation mechanism at the welding seam at the connection of the U-rib and top deck is discussed in this paper. First, a multiscale modeling method is established, including the whole bridge with a scale feature of  $10^2$  m, box girder components with a scale feature of  $10^0$  m, and cracks with a scale feature of  $10^{-3}$  m. A segmental model of the bridge deck at critical locations is extracted, and the shell-solid coupling method is adopted in the segmental model in order to further analyze the crack propagation rule. Afterwards, the fatigue cracks are statically and dynamically analyzed based on the XFEM. Finally, the thermoelastoplastic analysis of the welding seam between the U-rib and top deck is carried out. The life-and-death element technology is adopted to simulate the welding process, and the welding residual stress field is obtained. By introducing the results of the residual stress into the segmental model, the propagation rule of fatigue crack is studied, and the influences of welding residual stress and initial fatigue crack length and depth on fatigue crack propagation rule are further investigated.

## 2. Simulation Method of Fatigue Crack Propagation

**2.1. XFEM.** The XFEM is a modified finite element method proposed by Belytschko and Black [12] at Northwestern University in 1999, which is used to address discontinuity problems. The XFEM adopts the idea of partitioning the unity method to add the enrichment function that can reflect the displacement discontinuity into the displacement function of the conventional finite element. The displacement function of the XFEM method can be expressed as follows:

$$u(x) = \sum_{i \in N} N_i(x)u_i + \sum_{i \in N_T} N_i(x)H(x)a_i + \sum_{i \in N_A} N_i(x) \sum_{\alpha=1}^m \phi_\alpha(x)b_i^\alpha. \quad (1)$$

In the XFEM, the element grid is divided into three types, as shown in Figure 1: conventional finite elements, elements penetrated by cracks and elements with crack tips. The displacement functions of the corresponding elements include the displacement function of the conventional finite element, the enrichment function of the crack penetration element and the enrichment function of the element with a crack tip. In equation (1), the first term on the right is the displacement function of the conventional finite element,

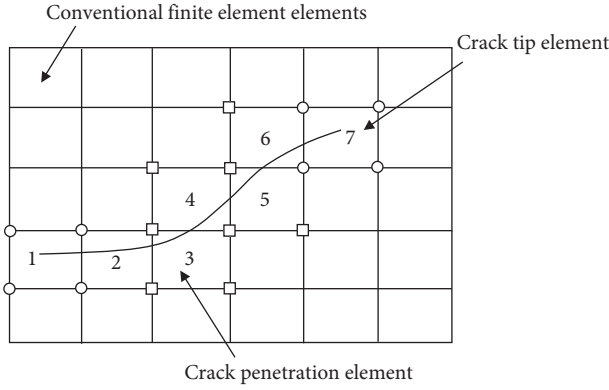


FIGURE 1: Element grid of XFEM.

the second term reflects the displacement discontinuity of the element penetrated by a crack, and the third term reflects the singularity of the crack tip, where  $u_i$  is the continuous nodal displacement,  $a_i$  and  $b_i^\alpha$  are the additional degrees of freedom for the nodes, and  $m$  is the number of the enrichment function at the crack tip.  $N_\Gamma$  is the nodal set contained in the elements penetrated by cracks, that is, the nodes contained in elements 2–6, as shown in Figure 1.

$N_\Delta$  is the nodal set contained in the elements with crack tips, that is, the nodes contained in elements 1 and 7, as shown in Figure 1.  $H(x)$  is the step function representing the discontinuous displacement fields on the upper and lower sides of the element penetrated by a crack, which can be expressed as follows:

$$H(x) = \begin{cases} +1, & (x - \bar{x}) > 0, \\ -1, & (x - \bar{x}) < 0. \end{cases} \quad (2)$$

In equation (1),  $\phi_\alpha(x)$  is the approximation function describing the displacement of the crack tip, which is composed of four basic functions and expressed as follows:

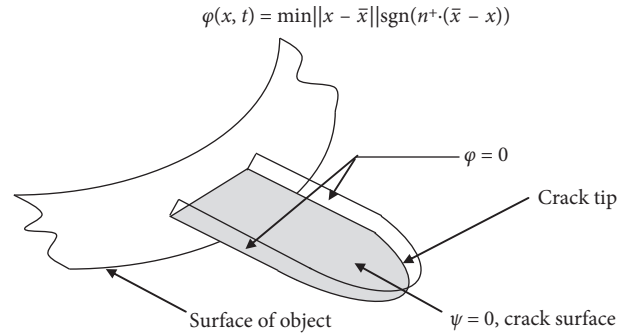
$$\phi_\alpha(x) = \begin{cases} \sqrt{r} \sin \frac{\theta}{2}, \sqrt{r} \cos \frac{\theta}{2}, \sqrt{r} \sin \theta \cos \frac{\theta}{2}, \\ \sqrt{r} \cos \theta \sin \frac{\theta}{2}, \end{cases} \quad \alpha = 1, 2, 3, 4. \quad (3)$$

In equation (3),  $(r, \theta)$  represents the polar coordinates of the crack tip.

In addition to introducing the enrichment function, the XFEM also uses the horizontal set function to determine the location of the crack to improve the computational efficiency [13–15]. For the plane cracks in the three-dimensional body, the normal level set function  $\psi$  and the tangent level set function  $\varphi$  perpendicular to each other are used to describe the cracks, as shown in Figure 2. The junction of  $\psi = 0$  and  $\varphi = 0$  is the crack tip. The tangent level set function  $\varphi$  can be expressed as follows:

$$\varphi(x, t) = \min \|x - \bar{x}\| \text{sgn}(n^+ \cdot (\bar{x} - x)), \quad (4)$$

where  $x = [x, y, z]$ ;  $\bar{x}$  is the projection of the coordinates of  $x$  on the crack surface;  $n^+$  is the external normal unit vector at


 FIGURE 2: Plane cracks represented by two level set functions  $\psi$  and  $\varphi$ .

the coordinates of  $x$  on the crack surface; and  $\text{sgn}(\cdot)$  is the sign function, as shown in equation (5). Similarly, the normal level set function  $\psi$  can be defined.

$$\text{sgn}(x) = \begin{cases} +1, & x > 0, \\ -1, & x < 0. \end{cases} \quad (5)$$

After the displacement function of the XFEM is obtained, the virtual work principle is used to calculate the virtual work equation of the structure with a crack, and then the control equation of the XFEM for the structure with cracks can be obtained by discretizing the virtual work equation.

Similar to the conventional finite element method, the XFEM solves the nodal displacement by the overall stiffness matrix of the element and the load matrix and then obtains the nodal stress. In contrast to the conventional finite element method, the XFEM adopts different integration methods for the different types of elements when solving the element stiffness matrix. Generally, the Gaussian integral method is adopted for conventional elements. Nevertheless, for an element penetrated by a crack and a crack tip element, because their displacement functions are discontinuous, their stiffness matrices are also discontinuous. In this case, these two types of elements are usually divided into several subelements bounded by crack edges, as shown in Figure 3. Figure 3(a) shows the subelements penetrated by crack, and Figure 3(b) shows the subelements with crack tip. And then, Gaussian integral method is adopted to obtain the stiffness matrices of these subelements. Eventually, the stiffness matrix of the element is obtained by summing the stiffness matrices of the subelements.

**2.2. Simulation Method of Fatigue Crack Propagation.** In the theory of LEFM, the Paris formula is commonly used to analyze fatigue crack propagation under cyclic loads, which can be expressed as follows:

$$\frac{da}{dN} = C(\Delta K)^m, \quad (6)$$

where  $a$  is the crack length;  $N$  is the cycle number;  $da/dN$  is the crack growth rate;  $C$  and  $m$  are material constants; and  $\Delta K$  is the amplitude of the SIF.

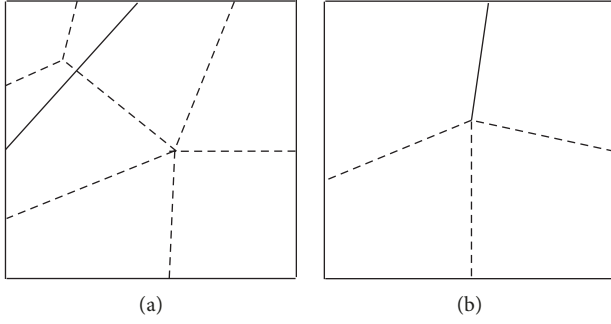


FIGURE 3: Element division for unconventional finite elements. (a) Subelements penetrated by crack. (b) Subelements with crack tip.

In the commercial finite element software ABAQUS, the Paris formula is expressed by the crack propagation rate and energy release rate, which can be written as follows:

$$\frac{da}{dN} = c_1 \Delta G^{c_2}, \quad (7)$$

where  $c_1$  and  $c_2$  are material constants and  $\Delta G$  is the amplitude of the energy release rate.

According to the relationship between the energy release rate  $G$  and SIF  $K$  in LEFM, equation (6) can be converted into equation (7), which can be written as follows:

$$G = \begin{cases} \frac{K^2}{E}, & \text{plane stress,} \\ \frac{(1-\nu^2)K^2}{E}, & \text{plane strain,} \end{cases} \quad (8)$$

where  $E$  is the material elastic modulus and  $\nu$  is Poisson's ratio.

When  $\Delta G$  is greater than  $G_{th}$  but less than  $G_{pl}$ , fatigue cracks begin to propagate. Here,  $G_{pl}$  is the maximum energy release rate, which is close to the fracture toughness  $G_C$  of steel.  $G_{th}$  is the threshold of the energy release rate. In this paper, the threshold of the SIF  $K_{th}$  of steel for a bridge is taken as  $92 \text{ MPa} \cdot \sqrt{\text{mm}}$  based on [16]. According to equation (8), the threshold of the energy release rate  $G_{th}$  can be obtained.

When the maximum energy release rate is greater than its threshold, fatigue cracks initiate and propagate. The crack propagation direction is the direction of the maximum shear stress of the crack tip element, and the fatigue crack propagation process is shown in Figure 4.

A refined model of the bridge containing an initial crack of length  $a_0$  was established. Under the  $j^{\text{th}}$  cyclic load, the maximum strain energy release rate is calculated to determine whether the crack propagates. If the maximum strain energy release rate is greater than the threshold  $G_{th}$ , the crack propagates; otherwise, the crack does not propagate, and the program ends. It is assumed that the  $i^{\text{th}}$  element in the crack front along the propagation direction happens to be cracking according to the normal level set function  $\psi$  and tangential level set function  $\phi$ , which are used to track the position of the virtual crack and determine the crack propagation length  $\Delta a_i$  of the  $i^{\text{th}}$  element. Virtual crack

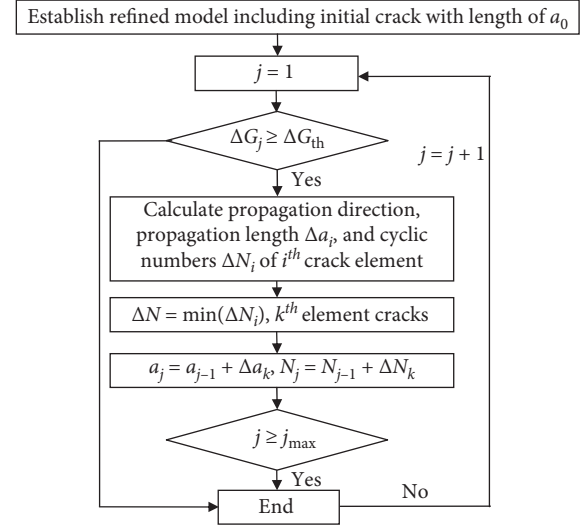


FIGURE 4: Simulation flow of the fatigue crack propagation process.

closure technology (VCCT) [17] is used to calculate the energy release rate  $\Delta G_i$  of the  $i^{\text{th}}$  element, and then the cyclic number increment  $\Delta N_i$  of the  $i^{\text{th}}$  element can be obtained by the integral form of the Paris formula. The element with the smallest increment of the cycle number begins to crack and is assumed to be the  $k^{\text{th}}$  element. The propagation length  $\Delta a_k$  and the increment of the cycle number  $\Delta N_k$  of the  $k^{\text{th}}$  element are recorded and the crack length  $a_j$  is updated to be equal to  $(a_{j-1} + \Delta a_k)$  and the cycle number  $N_j$  is equal to  $(N_{j-1} + \Delta N_k)$ . The next cycle is entered until the maximum number of cycles  $j_{max}$  set by the program is reached.

### 3. Numerical Simulations of Static Cracks at Different Critical Locations

**3.1. Finite Element Model.** A multiscale finite element model of the Runyang Yangtze River Highway cable-stayed bridge in China, as shown in Figure 5, is established by using the multiscale modeling method. Figure 5(a) shows the overall bridge model with a feature scale of  $10^2 \text{ m}$ ; Figure 5(b) shows the orthotropic steel bridge deck model with a feature scale of  $10^0 \text{ m}$ ; and Figures 5(c) and 5(d) show the semielliptical crack models in the weld toes of the U-rib and top deck, respectively, with a feature scale of  $10^{-3} \text{ m}$ . Considering that the midspan of the whole bridge may be the critical location [18] and the symmetry of the bridge along the lateral direction, a half model of the steel box girder with a length of 18.75 m in the midspan is selected as the standard segmental model, as shown in Figure 5(e). The shell-solid coupling method is adopted in the segmental model. In the segmental model, the shell element is used to simulate the inclined web, bottom plate and diaphragm plate, and the top plate and U-rib without crack, and the solid element is used to simulate the top plate and U-rib with crack. This is because the shell element cannot simulate cracks, only the solid element or two-dimensional plane element can do that. For the semielliptical crack at the welding toe of the U-rib and top deck, the SIF of the crack front is solved by the interaction integral to determine the

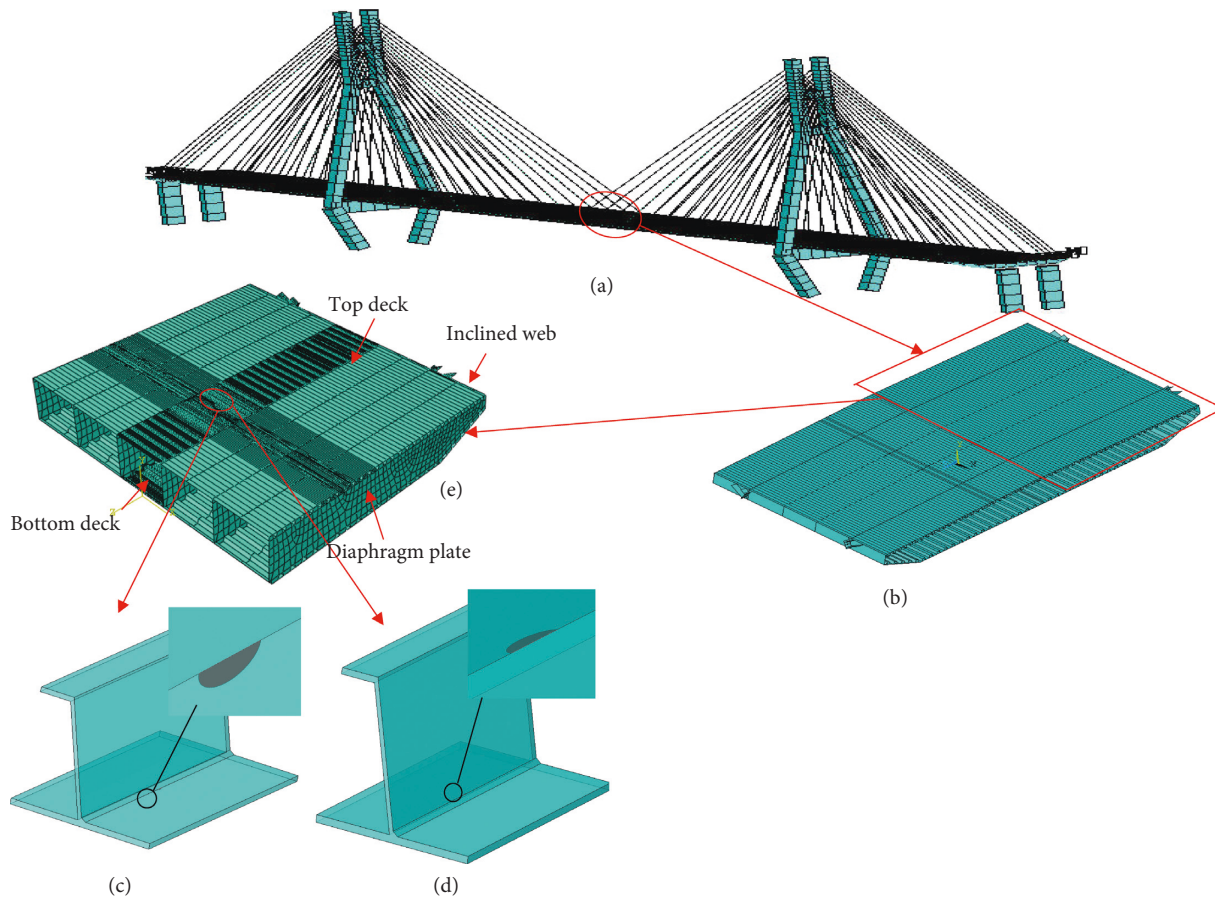


FIGURE 5: A multiscale finite element model of Runyang Yangtze River Highway Bridge. (a) Integral bridge model. (b) Orthotropic steel box girder including U-rib. (c) Crack at toe of top deck. (d) Crack at toe of U-rib. (e) Half of steel box girder model.

most unfavorable loading position that can drive the fatigue crack propagation.

The standard fatigue vehicle given in [19] is taken as the fatigue load, as shown in Figure 6, which is composed of four axles with a lateral wheelbase of 2 m and a longitudinal wheelbase of 6 m. Due to the large longitudinal wheelbase, for a specific node in the top deck of the bridge, when the front two wheels are located near this node, the rear two wheels are far away from the node and have little contribution to the fatigue stress of this node. Therefore, in this paper, only a vehicle with a longitudinal wheelbase of 1.2 m is taken as the fatigue load and applied to the segmental model. That is, the vehicle with an area of the wheel loading surface of  $0.2\text{ m} \times 0.6\text{ m}$  and a total weight of  $2 \times 120\text{ kN}$  is taken as the moving load adopted in this paper, as shown in Figure 6.

Figure 7 shows the loading cases of the model. Longitudinal loading cases, as shown in Figure 7(a), take their crack locations as the origins of the coordinates and the longitudinal direction of the bridge as the  $x$ -axis. The length from the front wheel to the crack position under the initial loading case is 250 mm; that is, the coordinates of the front wheel in this coordinate system are  $(-250\text{ mm}, 0)$ . The distance of the front wheel away from the crack under the final loading case is 350 mm; that is, under the final loading case, the coordinates of the front wheel are  $(+350\text{ mm}, 0)$ . The vehicle moves at 100 mm intervals in the  $x$ -axis positive

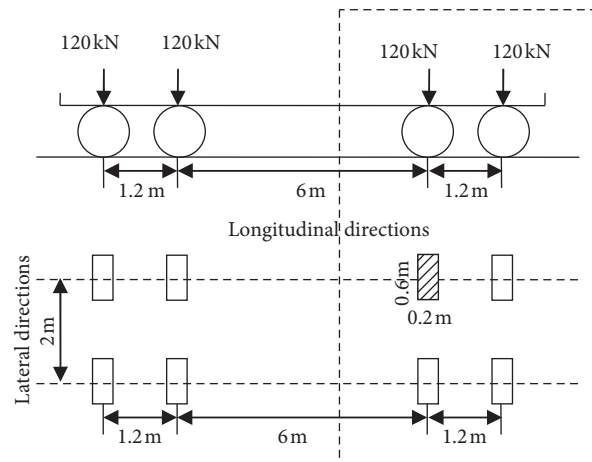


FIGURE 6: Standard fatigue load [19].

direction, eventually forming 7 longitudinal loading cases, called Z1-Z7. The lateral loading case is shown in Figure 7(b). When the wheel is close to the U-rib, the wheel moves at 100 mm intervals; that is, from loading cases H1 to H4 and H9 to H12, the vehicle moves at 100 mm intervals. When the wheel is far from the U-rib, the wheel moves at 200 mm or 300 mm intervals. For example, from H6 to H8, the vehicle moves at 300 mm intervals. From H4 to H5 and

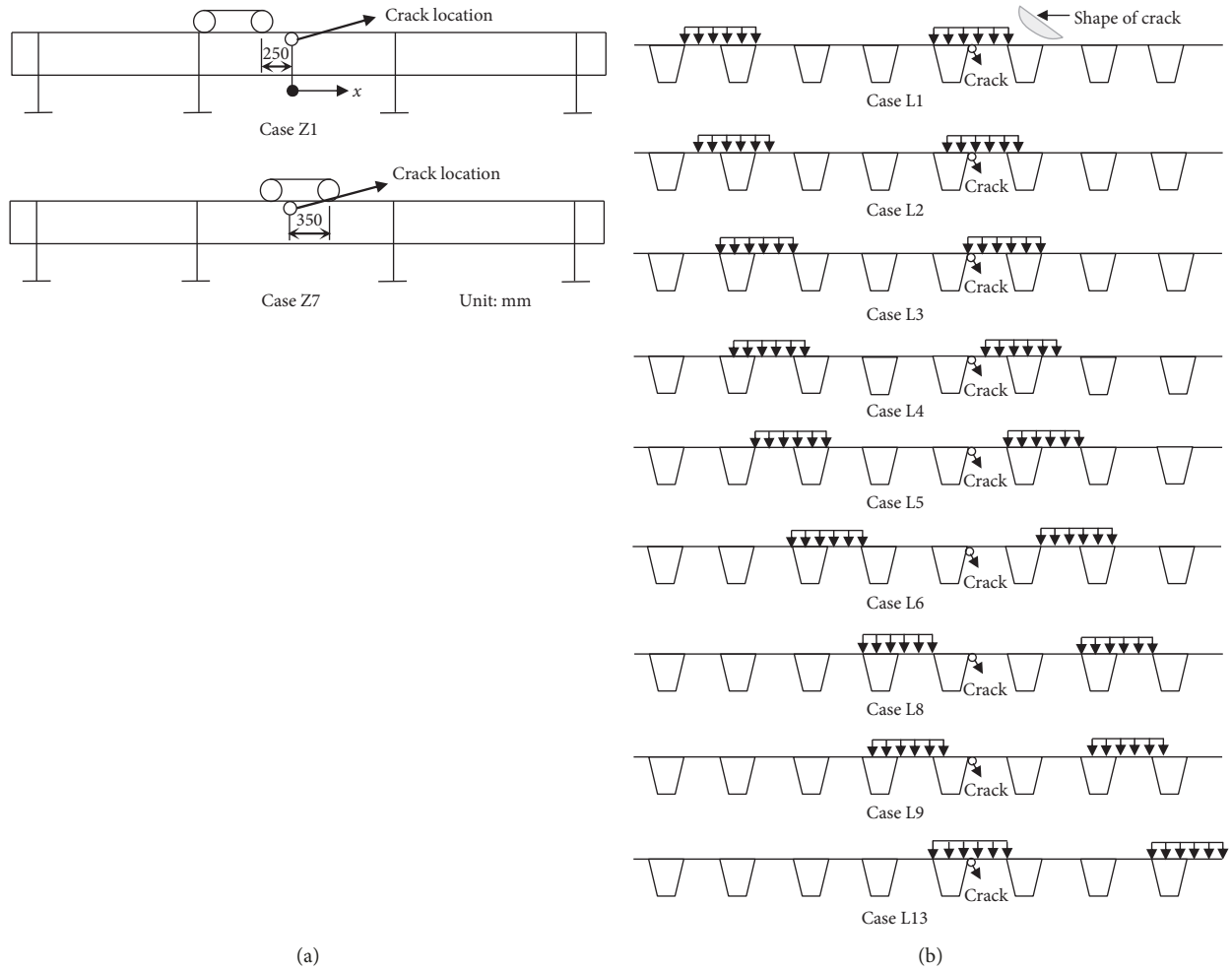


FIGURE 7: Loading cases. (a) Longitudinal loading cases. (b) Lateral loading cases.

from H12 to H13, the vehicle moves at 200 mm intervals. Finally, 13 lateral loading cases are formed.

**3.2. Solution of the SIF.** There are four types of fatigue cracks in the connection of the U-rib stiffened plate and top deck, as shown in Figure 8: (a) crack initiating from the root of the top deck toward the welding throat; (b) crack initiating from the welding toe of the top deck along the top deck; (c) crack initiating from the welding toe of the U-rib stiffened plate along the web of the U-rib; and (d) crack initiating from the root of the top deck toward the weld. By applying the vehicle load to the multiscale model of the bridge, the stress fields of the four types of fatigue cracks under the 13 loading cases can be obtained. Among the 13 loading cases, the maximum stress at the crack tip of four types is picked, and it is found that the stress at the crack tip of types (b) and (c) is higher than that of the other two types. We list out the maximum principal stress nephograms comparison for cracks of types (a) and (b) in Figure 9. Figure 9(a) shows the stress field distribution when the stress at the welding root reaches to the maximum under the 13 loading cases. Figure 9(b) shows the stress field distribution when the stress at the welding toe of top deck reaches to the maximum under the 13 loading

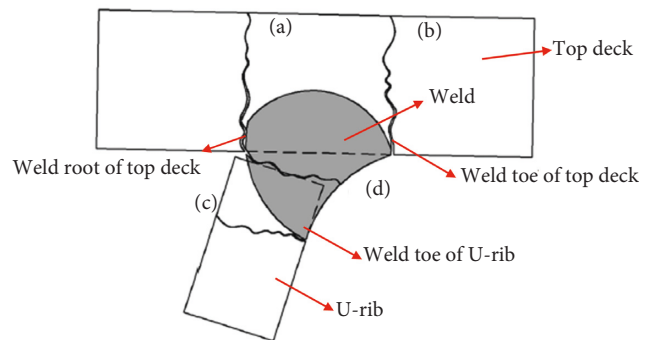


FIGURE 8: Four types of fatigue cracks in the connection of U-rib stiffened plate and top deck.

cases. It can be seen that the maximum stress for crack types (a) and (b) is 21.86 MPa and 29.98 MPa, respectively. Therefore, in this manuscript, the crack type (b) and (c) are selected for further study.

According to the stress characteristics and propagation paths of the cracks, the fracture modes of the cracks can be divided into three types: opening fracture mode, sliding fracture mode and tearing fracture mode, as shown in Figure 10. For the opening fracture mode (mode I crack), as

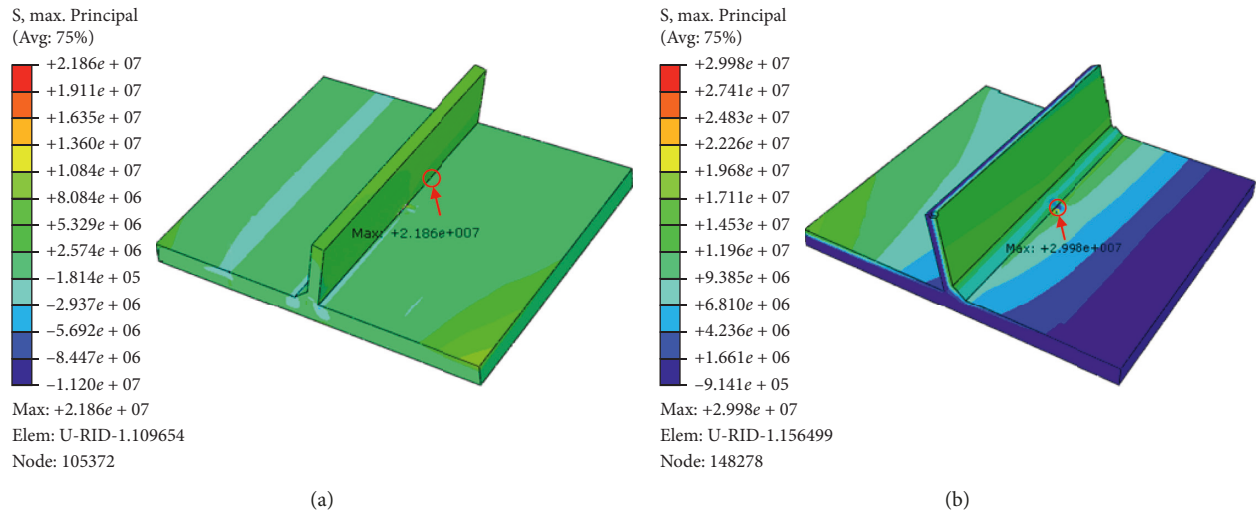


FIGURE 9: The maximum principal stress nephograms for crack type. (a) Crack from the welding root of top deck (type a) and (b) crack from the welding toe of top deck (type b).

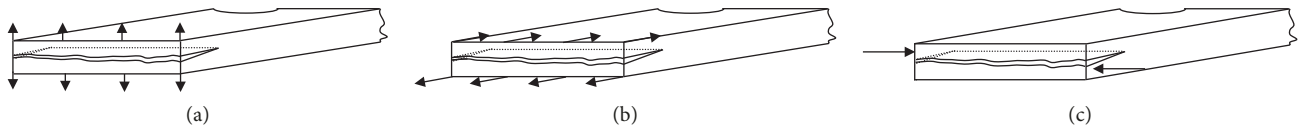


FIGURE 10: Three fracture modes: (a) opening fracture mode (mode I crack), (b) sliding fracture mode (mode II crack), and (c) tearing fracture mode (mode III crack).

shown in Figure 10(a), the tensile stress is perpendicular to the crack growth surface, and the crack propagates along the crack surface. For the sliding fracture mode (mode II crack), as shown in Figure 10(b), the crack is subjected to the shear stress, and propagates parallel to the crack surface. For the tearing fracture mode (mode III crack), as shown in Figure 10(c), under the action of the shear stress parallel to the crack surface and the crack front, the crack propagates along the tearing direction. Among them, mode I cracking is the most common but also the most dangerous fracture form. The steel bridge deck is usually in a complex stress state, so cracks often appear in the form of mixed-mode cracks.

According to the loading method mentioned in Section 3.1, static analysis for two types of cracks (b and c) in Figure 8 is carried out, and the SIFs at the crack tips of these two types of semielliptical cracks are calculated. The obtained SIF  $K_I$  is shown in Figure 11. Here, it is assumed that the half short axis length of the initial semielliptical crack is  $a_0$  and the length of the long axis is  $2c_0$ , and the ratio of  $a_0$  to  $(2c_0)$  is equal to 2.5 mm/10 mm, as shown in Figure 11(a).

Figure 11(a) shows the influence line of  $K_I$  for the mode I crack at the welding toe of the top deck. The valley value of  $K_I$  is approximately  $-183.6 \text{ MPa} \cdot \sqrt{\text{mm}}$ , indicating that the crack is in the closed state. The corresponding loading case is Z3-H2, namely, the right wheel of the front axle of the vehicle (see Figure 7) covers the crack surface of the top deck. The center of the right wheel is 50 mm away from the crack surface along the longitudinal direction and 100 mm

along the lateral direction. The peak value of  $K_I$  is approximately  $73.7 \text{ MPa} \cdot \sqrt{\text{mm}}$ , and the corresponding loading case is Z7-H12; that is, the left wheel center of the front axle is located 50 mm behind the crack surface and 500 mm at the left side. In this case, the crack opens, but the peak value does not reach the threshold of  $K_I$ . Therefore, the fatigue crack at the welding toe of the top deck will not propagate.

Figure 11(b) shows the influence line of  $K_I$  for the mode I crack at the welding toe of the U-rib stiffened plate. The peak value of  $K_I$  is  $107.5 \text{ MPa} \cdot \sqrt{\text{mm}}$  in the case of Z4-H9, and the valley value is  $-116.5 \text{ MPa} \cdot \sqrt{\text{mm}}$  in the case of Z4-H3. The peak value of  $K_I$  significantly exceeds the threshold value, indicating that the crack initiating at the welding toe of the U-rib stiffened plate has a strong driving force for crack propagation.

#### 4. Simulation of the Welding Processes of the U-Rib and Top Deck

4.1. Finite Element Model for Welding Analysis. During the welding process, the heat at the connection of U-rib and top deck will change rapidly with time and space, which is a typical nonlinear transient heat transfer problem. In this paper, in order to consider the effect of the welding residual stress on the static crack and dynamic crack propagation, thermoelastoplastic analysis is carried out for the joint of the U-rib and top deck. A bilinear isotropic strengthening model is established, and the incremental method is used to gradually solve the temperature fields and stress fields of the

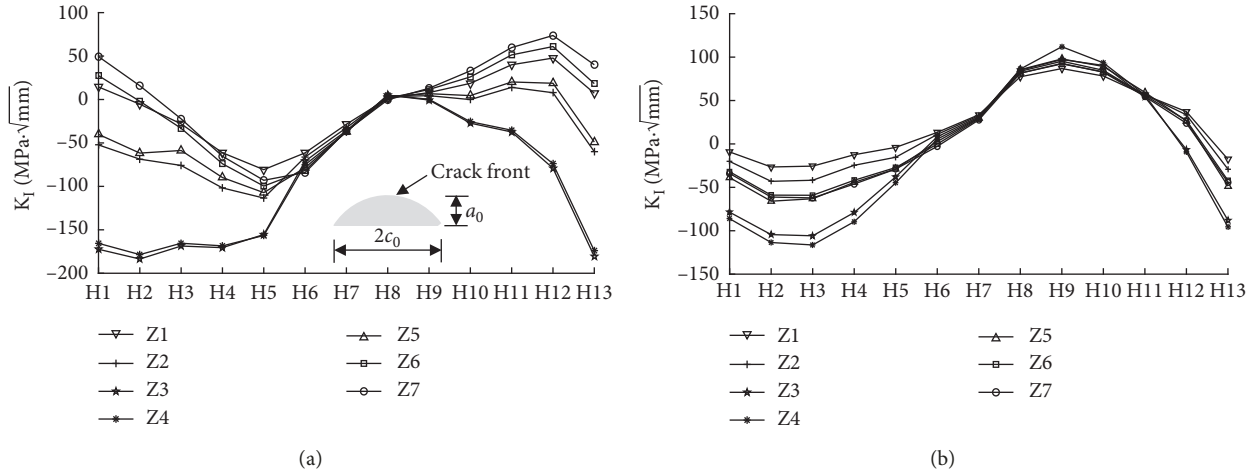


FIGURE 11: Influence line of  $K_I$  of the crack at the welding toes of the U-rib and top deck. (a) Crack at the welding toe of the top deck. (b) Crack at the welding toe of the U-rib web.

U-rib and top deck. The welding residual stress is solved by thermal analysis and order of the structural analysis.

The symmetry is used to simplify the model, and half of the U-rib and top deck is selected. The finite element model and boundary conditions are shown in Figure 12. The lateral length of the top deck is 300 mm, and the longitudinal length is 500 mm. The thermal analysis is first followed by the structural analysis, and the life-death element technique is adopted to complete the simulation of the welding process. The voltage of the welding heat source is taken as 250 V, the current is 25 A, and the thermal efficiency is 0.75. The ambient temperature is the same as the initial temperature of the component, which is set at 20°C. In the welding heating process, the heat source moves at a speed of 10 mm/s. For the U-rib with a length of 500 mm, the welding material melting process can be completed in 50 seconds. After the welding, the heat source is removed, and the temperature is gradually cooled to the initial temperature of the component, which takes 2100 seconds.

During the structure analysis, the  $z$ -direction symmetry constraint is applied to the central line of the top deck and U-rib, the translational displacement of the  $y$ -direction is restrained at the two sides of the top deck, and the  $x$ -direction displacement is restrained on one side of the cross-section of the top deck to simulate the construction support platform of the steel bridge deck.

The thermodynamical and mechanical parameters of steel in the welding process analysis are given in [20], and some of the data are properly modified to obtain the parameters applicable to this paper, as shown in Figure 13. Figure 13(a) shows the thermodynamical parameters, and Figure 13(b) shows the mechanical parameters.

**4.2. Results of the Welding Residual Stress.** The equivalent stress clouds at different times of the welding process are shown in Figure 14, namely, at 20 sec, 40 sec, 50 sec, and 2100 sec. Figure 14(a) shows the simulation result of this paper, and Figure 14(b) shows the simulation result in

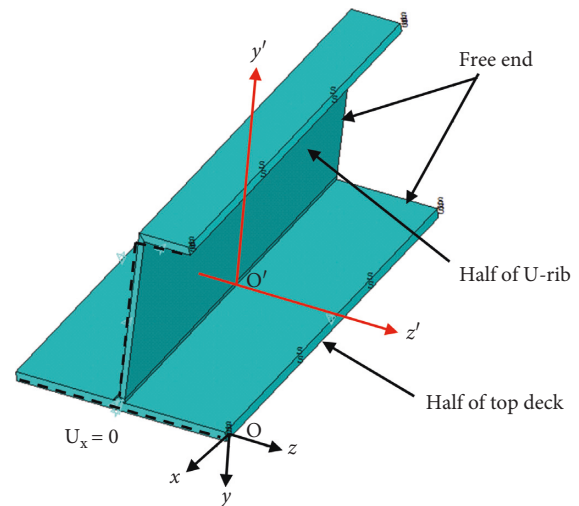


FIGURE 12: The finite element model and boundary conditions for welding analysis.

reference [8]. It can be observed that the simulation results are very close to each other, which verifies the accuracy of the results in this paper. During the movement of the heat source, the stress of the molten weld area is low, but the equivalent stress at the periphery of the weld is close to the yield stress of steel, and the maximum equivalent stress corresponding to 20 sec, 40 sec, and 50 sec reaches 368 MPa, 372 MPa, and 341 MPa, respectively. The stress of the whole weld area after the cooling period of 2100 sec reaches the yield stress of steel. Finally, there is a high residual stress in the weld zone.

Figure 15 shows the residual stress distribution at the 1/2 section of the U-rib and top deck. Figures 15(a) and 15(b) show the longitudinal residual stress of the top deck along the paths  $O'z'$  and  $O'y'$ , respectively, in Figure 12. As shown in Figure 14(a), the maximum longitudinal residual stress is located at a distance of 150 mm from the left; that is, the stress is basically located in the center of the weld seam. Residual stress is mainly tensile stress, and the maximum

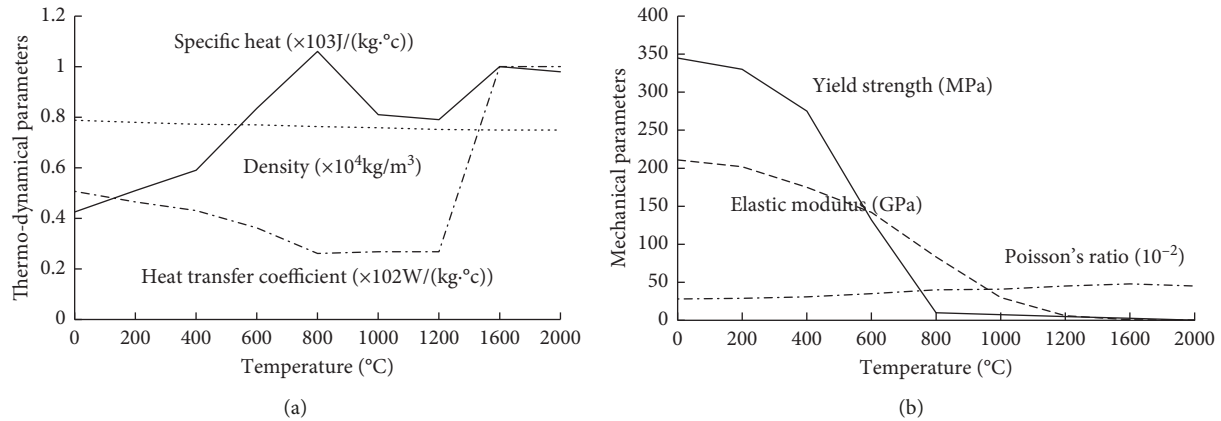


FIGURE 13: Thermal-dynamical and mechanical parameters of Q345 steel in welding process analysis. (a) Thermodynamical parameters. (b) Mechanical parameters.

value reaches the yield strength of steel. At the two ends of the top deck far away from the weld, the stress is compressive stress. Figure 14(b) shows that the longitudinal residual stress near the weld is tensile stress, and the value is slightly higher than the yield stress of steel. The farther the stress from the weld, the smaller the stress. The residual stress is transformed into compressive stress at a certain distance away from the weld.

## 5. Numerical Simulation of Fatigue Crack Propagation

**5.1. Crack Propagation Analysis at the Weld Toe of the U-Rib Web.** According to the results of the static analysis of the fatigue crack in Section 3.2, the stress field at the crack tip of the weld toe of the U-rib web has enough driving force to drive the crack growth for the most unfavorable loading case of Z4-H9. Therefore, for this most unfavorable case, the dynamic propagation of fatigue cracks is further studied. To improve the calculation efficiency, this paper analyzes the fatigue crack propagation at the toe of the U-rib under 200 cycles and compares the difference between the crack propagations of the two cases with and without a residual stress field. It is assumed that the half short axis length of the initial semielliptical crack is  $a_0$  and the length of the long axis is  $2c_0$ , and the ratio of  $a_0$  to  $(2c_0)$  is equal to 2.5 mm/10 mm. The morphology of crack propagation without residual stress field and with residual stress field is shown in Figure 16.

Figures 16(a) and 16(b) show that the fatigue crack at the weld toe of the U-rib web propagates to the height of the web, but the angle is different. When the residual stress field is not taken into account, the fatigue crack propagates along the direction of its length and turns slightly to the direction of the U-rib under the action of the vehicle load. When the fatigue crack propagation is approximately 12.5 mm, the SIF of the new crack tip is low and does not reach the threshold value in the specification, and the fatigue crack stops propagating. After introducing the residual stress field, the fatigue crack propagates in the directions of the length and depth, and the upper right

graph of Figure 16(b) shows that the fatigue crack has penetrated through the thickness of the U-rib. Comparing the analysis results with and without a residual stress field, it can be found that the angle and length of fatigue crack propagation under the residual stress field are notably larger than those without a residual stress field, and there is no crack stopping phenomenon.

The cumulative strain energy release rate during the process of crack propagation is shown in Figure 17. It can be seen that  $G_{II}$  is close to  $G_{III}$ . The ratio of  $G_I$  to  $G_{II}$  decreases with increasing cycle number. At the end of the cycle, the ratio of  $G_{II}$  to  $G_I$  is approximately 0.2. Therefore, for a cycle number of 200, the fatigue crack is a mixed-mode I-II-III crack. The influence of the mode II fracture and mode III fracture on crack propagation cannot be ignored, which will cause crack deflection in the process of crack propagation, and the deflection angle will increase with the increase in the cycle number.

**5.2. Analysis of Crack Propagation at Welding Toe of Top Deck.** The static analysis of the fatigue crack shows that the stress at the crack tip of the weld toe of the top deck could not drive the crack propagation when it was subjected to the most unfavorable loading conditions without a residual stress field. Therefore, to study the crack propagation at the weld toe of the top deck, it is necessary to consider the existence of a residual stress field. Here, we still assume that the short axis length of the initial semielliptical crack is  $a_0$ , the length of the long axis is  $c_0$ , and the ratio of  $a_0$  to  $(2c_0)$  is equal to 2.5 mm/10 mm. The morphology of crack propagation of the top deck is shown in Figure 18.

Figure 18(a) shows the simulation result of this paper, and Figure 18(b) shows the simulation result in reference [6]. The shapes of the crack surfaces are very similar, which validates the accuracy of the simulation results in this paper. The upper right corner of Figure 18(a) is the deformation diagram of the crack surface. The fatigue crack at the weld toe of the top deck propagates along the length direction of the deck and at the end of the cycle, the crack propagates to the weld zone. From the undeformed figure in the lower

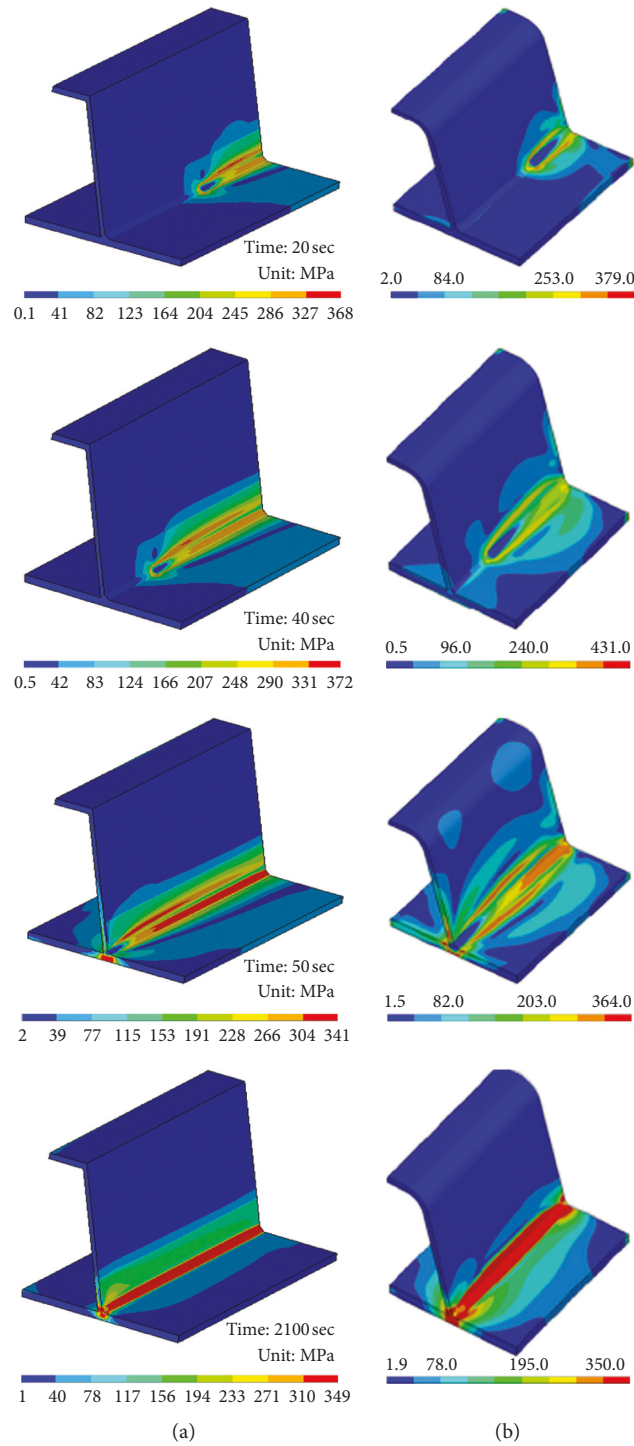


FIGURE 14: The equivalent stress clouds at different times of the welding process at the connection of the U-rib and the top deck. (a) The simulation result in this paper. (b) Results in reference [8].

right corner of Figure 18(a), it can be seen that the fatigue crack propagates in both the length and depth, and the shape of the crack surface changes with the number of cycles but remains semielliptical.

Figure 19 shows the cumulative strain energy release rate at the welding toe of the top deck. The opening fracture mode dominates, and the strain energy release rate of mode II is approximately two times that of mode III. The ratio of

$G_{II}$  to  $G_I$  is 0.017, and that of  $G_{III}$  to  $G_I$  is 0.035, respectively. The ratios are small but the sliding fracture mode and tearing fracture mode will cause a small deflection of the crack propagation direction.

5.3. Analysis of Crack Propagation with Different Sizes in the Residual Stress Field. Considering the influence of the residual stress field, different semielliptical initial cracks with

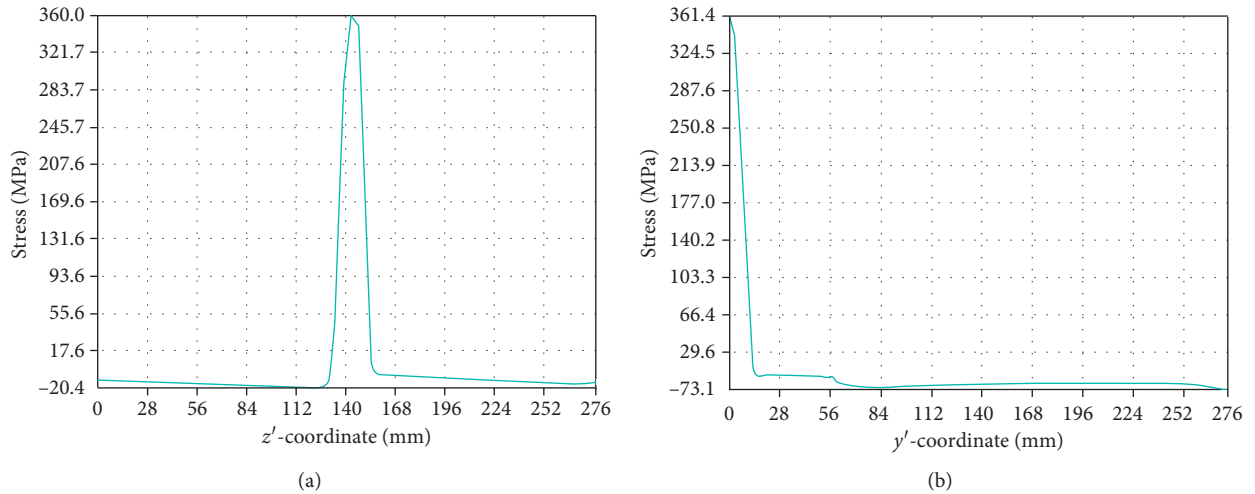


FIGURE 15: The residual stress distribution at 1/2 section of the U-rib and top deck. (a) The longitudinal residual stress of the top deck. (b) The longitudinal residual stress of the U-rib.

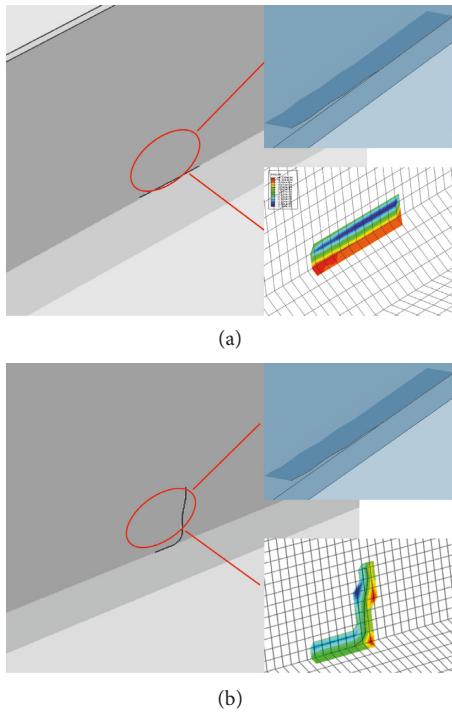


FIGURE 16: The morphology of crack propagation at the welding toe of U-rib. (a) Without residual stress field. (b) With residual stress field.

ratios of  $a_0$  to  $(2c_0)$  of 2.5 mm/10 mm, 2.5 mm/15 mm, and 4 mm/10 mm are established at the welding toe of the top deck for fatigue crack propagation analysis. Figure 20 shows the morphology of crack propagation after the end of the cycle.

The propagation behavior of the initial crack with the first two sizes is the same, and the crack surface basically maintains a semielliptical shape during the process of propagation. Nevertheless, the crack with a ratio of  $a_0$  to  $(2c_0)$  of 4 mm/10 mm has a different propagation shape

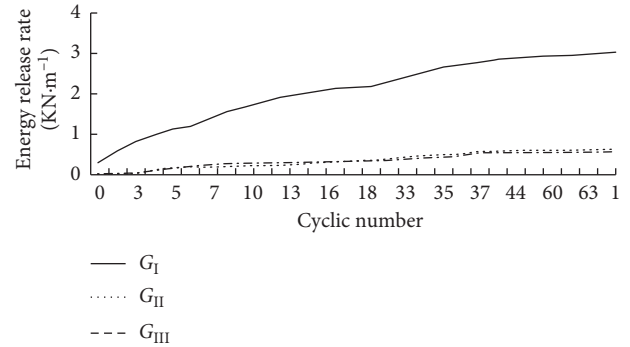


FIGURE 17: The cumulative strain energy release rate during the process of crack propagation at the welding toe of U-rib.

along the depth direction. As the welding residual stress has certain stress gradients in the directions of the thickness and length of the plate, and the stress of the mother plate close to the weld area is high, this situation leads to a deflection of the crack in the depth direction and the deflection angle gradually increases and finally causes the crack surface in the depth direction almost to be parallel to the edge of the top deck.

Figure 21 shows the relationship between the number of cracking elements and load cycle numbers, which can indirectly reflect the fatigue crack propagation rate. The number of cracking elements can indirectly indicate the length of crack propagation. When the number of loading cycles is smaller than 10, the number of cracking elements of the three initial cracks is similar to the number of cycles, and this phase reflects the propagation of the crack along the length direction. When the crack in the weld toe of the top deck propagates to the weld zone along the length, the stress field at the crack tip cannot drive the crack to continue to propagate along the length direction; thus, the crack begins to propagate in the depth direction. Figure 21 shows that for the same cycle numbers, the number of cracking elements with a ratio of  $a_0$  to  $(2c_0)$  of 4 mm/10 mm is the largest, that

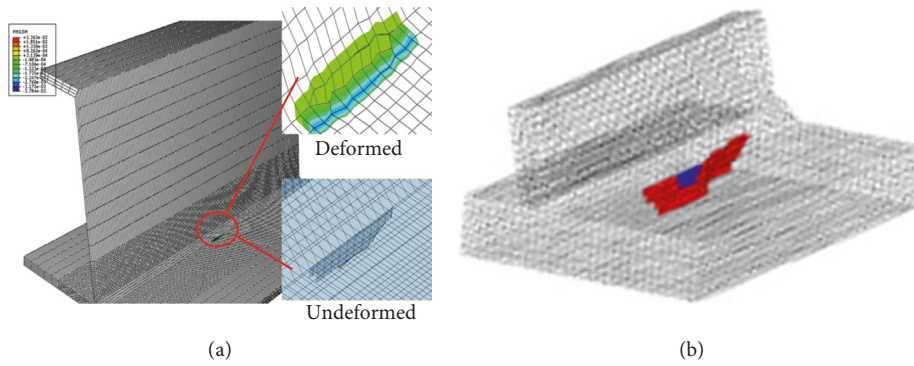


FIGURE 18: The morphology of crack propagation at the welding toe of top deck: (a) simulation result in this paper; (b) result in reference [6].

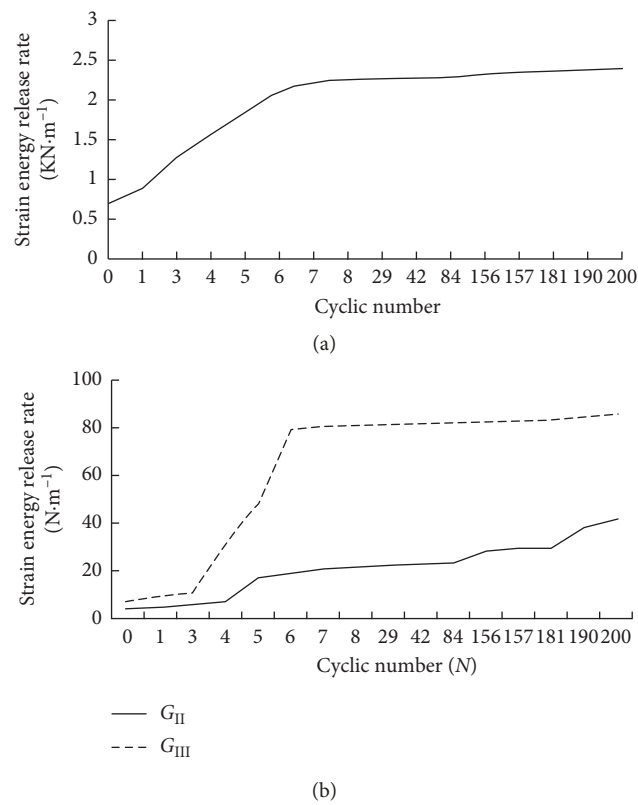


FIGURE 19: The cumulative strain energy release rate at the welding toe of top deck. (a) Opening fracture mode (Mode I crack). (b) Sliding and tearing fracture modes (Mode II and III cracks, respectively).

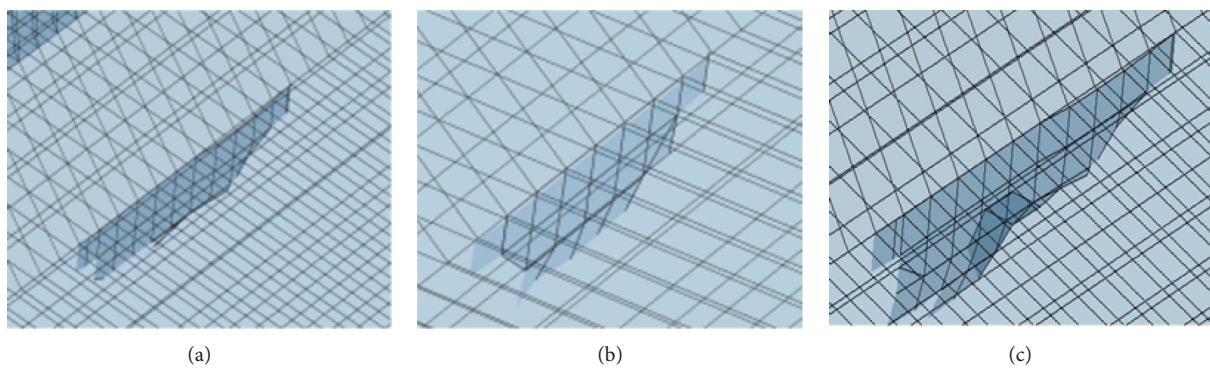


FIGURE 20: The morphology of crack propagation after the end of the cycle. (a) 2.5 mm/10 mm. (b) 2.5 mm/15 mm. (c) 4 mm/10 mm.

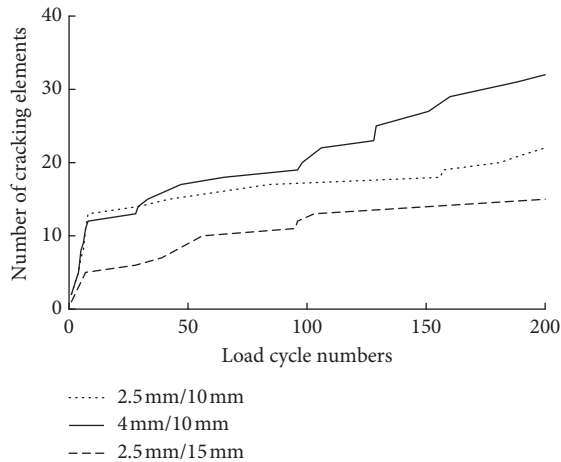


FIGURE 21: The relationship between the number of cracking elements and load cycle numbers.

is, the fastest crack growth rate, followed by the initial crack with a ratio of  $a_0$  to  $(2c_0)$  of 2.5 mm/10 mm. Although the initial crack with a ratio of  $a_0$  to  $(2c_0)$  of 2.5 mm/15 mm is the longest, under 200 load cycles, the crack has the lowest crack propagation rate.

## 6. Conclusions

The fatigue cracking problem at the weld toe of the U-rib and top deck is discussed in this paper. The fatigue crack propagation mechanism of the weld toe under a vehicle load was studied based on the XFEM, and the influence of the welding residual stress field on crack propagation was further investigated. The following conclusions were obtained:

- (1) The calculated SIF at the crack tip at the weld toe of the top deck under the action of a standard vehicle fatigue load is lower than the SIF threshold of steel; as a result, the crack will not propagate. Residual stress analysis of the welding process shows that the peak of the residual tensile stress at the U-rib and top deck joint can reach the material yield strength. After the residual stress field is introduced, the fatigue crack at the weld toe of the top deck is a mixed-mode I-II-III crack, which is dominated by the opening fracture mode. The sliding fracture mode and tearing fracture mode will lead to a small deflection of the fatigue crack to the weld throat area.
- (2) Under the action of a standard vehicle load, the crack at the weld toe of the U-rib will propagate because the stress field of the crack tip has enough driving force to drive its propagation. The crack tip extends to approximately 12.5 mm along the length of the U-rib until the stress in the stress field at the new crack tip is reduced to a new low level, and the fatigue crack stops. After the residual stress is taken into account, the fatigue crack extends in the directions of the crack length and depth, and the angle between the crack and weld length increases with increasing crack propagation.

- (3) Under a low cyclic load, the initial crack size at the weld toe of the top deck in the residual stress field will affect the crack propagation rate. Compared to the crack length, the initial crack depth has a larger effect on the rate, and the size of the initial depth will have a direct impact on the rate.

## Data Availability

The data used to support the findings of this study are included within the supplementary information files.

## Conflicts of Interest

The authors declare that they have no conflicts of interest.

## Acknowledgments

The works described in this paper are substantially supported by the grant from the National Natural Science Foundation of China (grant no. 51678135); the Natural Science Foundation of Jiangsu Province (no. BK20171350); the Fundamental Research Funds for the Central Universities (no. 2242016R30009); the Priority Academic Program Development of Jiangsu Higher Education Institutions (PAPD), the Top-Notch Academic Program Project of Jiangsu Higher Education Institutions (TAPP); and the Six Talent Peak Projects in Jiangsu Province (JNHB-007), which are gratefully acknowledged.

## Supplementary Materials

S1: the original data used to plot the influence line of KI of the crack at the welding toe of top deck in Figure 11(a), to plot the influence line of KI of the crack at the welding toe of U-rib web in Figure 11(b), to obtain the thermal-dynamical and mechanical parameters of Q345 steel in welding process analysis showing in Figure 13, to obtain the change of the cumulative stain energy release rates with cyclic numbers at the welding toe of U-rib in Figure 17, to obtain the change of the cumulative stain energy release rates with cyclic numbers at the welding toe of top deck in Figure 19, and to obtain the change of numbers of crack elements with the cycle numbers under the different crack length in Figure 21. (*Supplementary Materials*)

## References

- [1] Y. Wang and Y. Q. Zheng, "Simulation of damage evolution and study of multi-fatigue source fracture of steel wire in bridge cables under the action of pre-corrosion and fatigue," *CMES-Computer Modeling in Engineering & Sciences*, 2019.
- [2] C. Wang, L. Duan, M. Zhai, Y. Zhang, and S. Wang, "Steel bridge long-term performance research technology framework and research progress," *Advances in Structural Engineering*, vol. 20, no. 1, pp. 51–68, 2017.
- [3] D. S. He, H. Z. Xiao, and X. Y. Zhang, "Research on detail fatigue of orthotropic steel deck in Highway bridge," *Journal of Highway and Transportation Research and Development*, vol. 33, no. 1, pp. 76–81, 2016.

- [4] J. W. Fisher, *Fatigue and Fracture in Steel Bridges*, John Wiley & Sons, New York, NY, USA, 1984.
- [5] Q. H. Zhang, Z. K. Jin, Y. M. Liu, and Y.-Z. Bu, "3-D Simulation method for fatigue crack propagation in rib-to-deck welded joints of orthotropic steel bridge deck," *China Journal of Highway and Transport*, vol. 31, no. 1, pp. 57–66, 2018.
- [6] C. S. Wang, B. N. Fu, Q. Zhang, and Y.-C. Feng, "Fatigue test on full-scale orthotropic steel bridge deck," *China Journal of Highway and Transportation*, vol. 26, no. 2, pp. 69–76, 2013.
- [7] C. S. Wang, M. S. Zhai, Y. M. Tang, W.-Z. Chen, and T.-Y. Qu, "Numerical fracture mechanical simulation of fatigue crack coupled propagation mechanism for steel bridge deck," *China Journal Highway Transportation*, vol. 30, no. 3, pp. 82–95, 2017.
- [8] W. Nagy, P. Van Bogaert, and H. De Backer, "LEFM based fatigue design for welded connections in orthotropic steel bridge decks," *Procedia Engineering*, vol. 133, pp. 758–769, 2015.
- [9] W. Nagy, K. Schotte, P. Van Bogaert, and H. De Backer, "Fatigue strength application of fracture mechanics to orthotropic steel decks," *Advances in Structural Engineering*, vol. 19, no. 11, pp. 1696–1709, 2016.
- [10] B. Wang, X.-Y. Zhou, H. De Backer, A. Chen, and F. Schmidt, "Macro-crack initiation life for orthotropic steel decks considering weld heterogeneity and random traffic loading," *Structure and Infrastructure Engineering*, vol. 13, no. 12, pp. 1639–1652, 2017.
- [11] Q. Du and G. Y. Shi, "Crack growth analysis of the rib -to-deck welded joints of orthotropic steel deck under cyclic loading with negative stress ratio," *Chinese Journal of Computational Mechanics*, vol. 34, no. 6, pp. 698–703, 2017.
- [12] T. Belytschko and T. Black, "Elastic crack growth in finite elements with minimal remeshing," *International Journal for Numerical Methods in Engineering*, vol. 45, no. 5, pp. 601–620, 1999.
- [13] L. L. Guo, Z. F. Chen, J. R. Luo, and G. Chen, "A review of the extended finite element method and its applications," *Chinese Quarterly of Mechanics*, vol. 32, no. 4, pp. 612–625, 2011.
- [14] T. T. Yu, *Theory, Application and Program of Extended Finite Element Method*, Science Press, Beijing, China, 2017, in Chinese.
- [15] I. V. Singh, B. K. Mishra, S. Bhattacharya, and R. U. Patil, "The numerical simulation of fatigue crack growth using extended finite element method," *International Journal of Fatigue*, vol. 36, no. 1, pp. 109–119, 2012.
- [16] Japan Society of Steel Construction (JSSC), *Fatigue Design Recommendations for Steel Structures and Commentary*, Japan Society of Steel Construction (JSSC), Tokyo, Japan, 1993.
- [17] T. Xiao, Z. X. Zuo, D. Liu et al., "Computation of the crack propagation energy release rate based on the virtual crack closure technique," *Transactions of Beijing Institute of Technology*, vol. 30, no. 1, pp. 37–41, 2010.
- [18] Y. Wang, "Research on fatigue condition assessment method of steel box girder for long-span cable-supported bridges," Doctoral dissertation, Southeast University, Nanjing, China, 2009.
- [19] China Communication Press, *JTG D64-2015 Specification for Design of Highway Steel Bridge*, China Communication Press, Beijing, China, 2015.
- [20] Q. Zhao and C. Wu, "Numerical analysis of welding residual stress of U-rib stiffened plate," *Engineering Mechanics*, vol. 29, no. 8, pp. 262–268, 2012.



**Hindawi**

Submit your manuscripts at  
[www.hindawi.com](http://www.hindawi.com)

